Research Article

Real-Time and Highly Sensitive Detection of Matrix Metalloproteinase 9 (MMP-9) in Tears Using Aptamer Functionalized Electrolyte-Gated IGZO Thin-Film Transistors

Chuljin Hwang, Jee Hoon Lee, Dong-Kyu Kim, Kyung-Sun Na,* and Dae Yu Kim*

Cite This: *ACS Appl. Mater. Interfaces* 2025, 17, 38848−38858
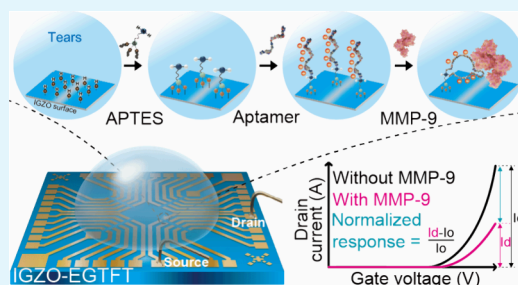
Read Online

ACCESS | Metrics & More | Article Recommendations | SI Supporting Information

ABSTRACT: Dry eye disease (DED) is a common disorder characterized by unstable tear film homeostasis. Its symptoms range from foreign body sensations to pain and fluctuations in visual function. Current diagnostics include physical examination and ocular surface imaging. Matrix metalloproteinase-9 (MMP-9) in tears correlates with clinical signs of DED; however, because of the limited sample volume, quantitative and real-time detection of MMP-9 is a significant need, complicated by the biochemical complexity of tears. We developed an ultrasensitive, real-time MMP-9 sensor based on electrolyte-gated indium−gallium−zinc oxide thin-film transistors (IGZO-EGTFTs), capable of analyzing submicroliter sample volumes. The sensor surface was functionalized at the nanoscale to improve the binding capability of the aptamer, achieving a limit of detection of 1 fg/mL. The sensor demonstrated excellent reproducibility over a dynamic detection range spanning 8 orders of magnitude up to 100 ng/mL (10^{-7} g/mL), which was consistent with the clinical range of DED patients. Additionally, the sensing performance remained stable for up to 4 weeks, highlighting its potential for future commercial applications. The MMP-9 concentration in human tear samples could be determined by the developed sensor in real time with high sensitivity, which provides promising diagnostic tools for early detection, progression assessment, and timely treatment of DED.

KEYWORDS: *indium−gallium−zinc oxide sensor, electrolyte-gated thin-film transistor, dry eye disease, matrix metalloproteinase-9 sensor, IGZO-EGTFT*

1. INTRODUCTION

Dry eye disease (DED) is a common disorder characterized by disrupted tear-film homeostasis. Its etiology involves tear-film instability, hyperosmolarity, ocular surface inflammation, and neurosensory abnormalities.[1] DED symptoms include severe pain and fluctuations in vision, which can significantly reduce quality of life.[2−5] The global incidence of DED ranges from 5 to 50%, with approximately 16 million patients in the U.S. and 0.4−3.7 billion patients worldwide.[6−8] Current diagnostic methods include measuring tear film breakup time (tBUT), fluorescein or lissamine green staining of the cornea and conjunctiva, and the Schirmer test. However, all of these have low specificity and interobserver variability,[9−12] complicating assessment.[13] The absence of a gold-standard test impairs diagnostic accuracy;[14] Therefore, identifying objective and measurable biomarkers is essential for improving DED diagnostic accuracy, prevention, and treatment.

The matrix metalloproteinases (MMPs) are a family of proteolytic enzymes that play crucial roles in physiological and pathophysiological tissue remodeling. In vertebrates, 25 family members have been identified, with 22 present in humans.[15,16] Among these, MMP-9 is secreted by the corneal epithelium, with its concentration in tears showing strong correlations with DED symptoms.[17] Elevated MMP-9 levels compromise corneal epithelium barrier function, leading to ocular surface inflammation.[18] These findings indicate that the concentration of MMP-9 in the tear fluid can serve as a useful biomarker for diagnosis, prognosis, and treatment of DED.[19]

InflammaDry (Quidel Eye Health, San Diego, CA, USA) is the only US Food and Drug Administration-approved test specifically designed to detect both active and latent MMP-9 in tears.[20] The test provides a binary result indicating whether the MMP-9 concentration exceeds 40 ng/mL, achieving 85% sensitivity and 94% specificity.[21] However, it does not measure precise MMP-9 concentrations, making it less useful. The measurement does not merely depend on the band density related to tear volume (>20 μL) but also incubation time for the chemical reaction.[22] In addition, the test lines are read by
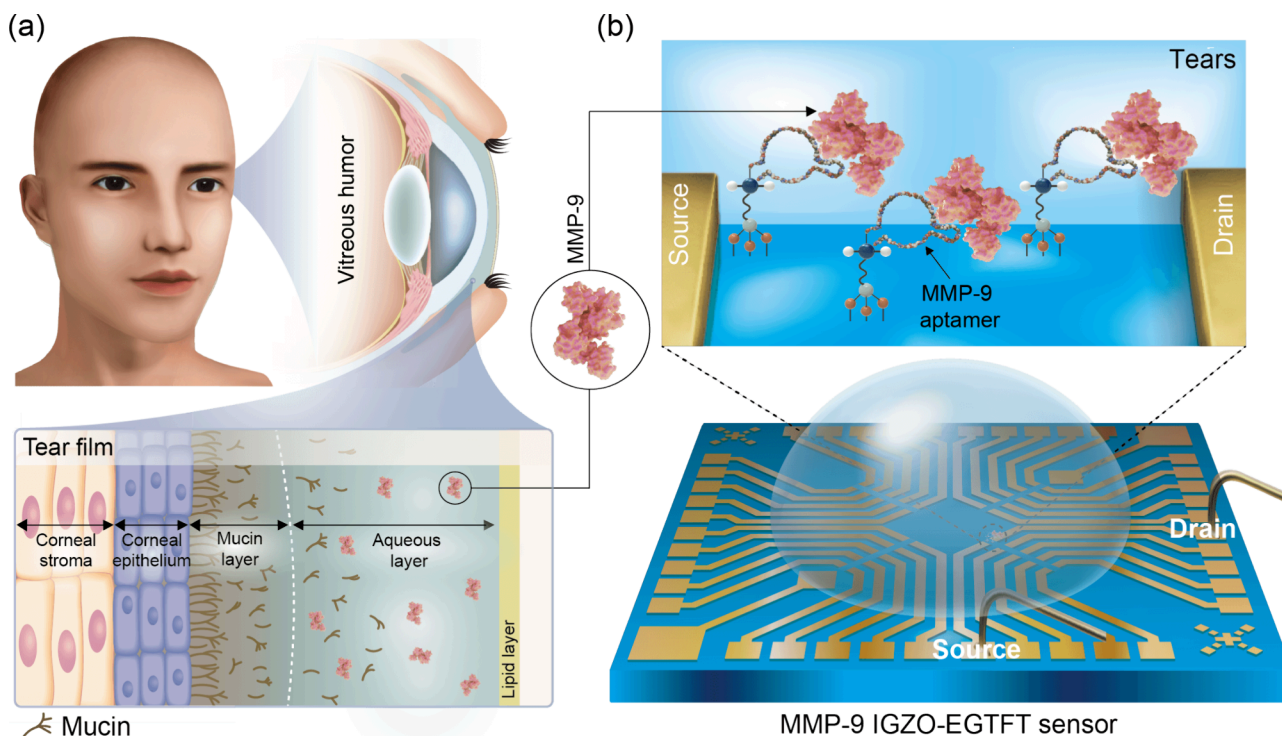
Scheme 1. Design Concept of MMP-9 IGZO-EGTFT Sensor[a]

[a](a) Representation of the ocular surface composition and MMP-9 in tear film; (b) schematic diagram of developed sensors based on the IGZO-EGTFTs for detecting MMP-9 in human tear samples.

the unaided human eye, reducing accuracy. An enzyme-linked immunosorbent assay (ELISA) is a second method for the quantification of MMP-9; however, it also has shortcomings such as poor repeatability, low sensitivity, long incubation time, and dependence on fluorescent labeling skills, particularly important for early DED diagnosis.[23−26]

Electrolyte-gate thin-film transistors (EGTFT) based on metal-oxide semiconductors have potential as alternative test platforms for detecting MMP-9. Their high electrical double-layer (EDL) capacitance formed at the electrolyte-semiconductor interface facilitates sensitive and rapid detection at low operating voltages below 1 V. The low operating voltage prevents water electrolysis and ensures stable operation in aqueous environments, achieving a high signal-to-noise ratio in multiple biological solutions, including tears, urine, and serum.[27−30] As a metal-oxide sensing layer, IGZO has attracted considerable attention owing to its high electrical mobility, rapid transient response, large current on/off ratio, chemical stability, and large-area process at relatively low temperatures.[31−35] Furthermore, the surface of IGZO can be readily functionalized using conventional organosilane-based chemistry and cross-linking reactions forming a stable biochemical interface.[36] Such surface functionalization facilitates efficient immobilization of biorecognition elements such as enzymes, antibodies, and aptamers on the IGZO surface allowing direct and sensitive transduction of specific biological interactions into amplified electrical signals.[37,38] For example, Chae et al.[39] demonstrated the repeatability and stability of IGZO-EGTFTs as biological sensing platforms to detect α-synuclein in electrolyte solutions. Monoclonal antibodies were employed as bioreceptors, achieving quantitative detection of α-synuclein from 10 fg/mL to 1 ng/mL.

However, quantitative and real-time detection of MMP-9 for the accurate diagnosis of DED remains a significant challenge due to the limited tear volume and the extremely low concentration of MMP-9. Furthermore, as highlighted in a recent review,[40] the biochemical complexity of tear fluid, which includes lipids, immunoglobulins, proteins, mucins, and ions, can interfere with clinically reliable, label-free, and selective detection. These challenges can be addressed by optimizing nanoscale surface functionalization to enhance target recognition efficiency and by integrating bioreceptors directly at the solid−electrolyte interface to improve detection specificity and stability. Collectively, these approaches enable real-time detection which is particularly important for measuring transient inflammatory changes in DED and supporting timely diagnosis as well as treatment assessment.

In this study, we developed a label-free and real-time MMP-9 sensor based on IGZO-EGTFTs for the ultrasensitive and quantitative detection of MMP-9 in human tears (Scheme 1). Through precisely controlled surface modification, the surface of IGZO was functionalized to facilitate the stable covalent immobilization of aptamers. The specific binding interaction between MMP-9 and the immobilized aptamers on the IGZO surface significantly enhanced the sensitivity of the sensor, achieving an impressively low detection limit of 1 fg/mL with high specificity using an ultralow sample volume of 1 μL (substantially lower than the 100 μL typically required in conventional ELISA assays.). Additionally, the MMP-9 was detected in real-time across a broad linear range from 1 fg/mL to 100 ng/mL (R^2 = 0.996) MMP-9 with long-term stability (up to 4 weeks), which was satisfied with the clinical range for DED patients. The performance and reliability of sensors were further validated using undiluted tear samples collected from DED patients and cross-verified against results obtained from

commercially available InflammaDry kits. Hence, it is expected that proposed sensors have the potential to serve as point-of-care devices, enabling assessment of inflammation severity and ultimately facilitating early detection and timely treatment for DED patients beyond simple diagnosis.

2. MATERIALS AND METHODS

2.1. Reagents and Materials. Indium nitrate hydrate (In $(NO_3)_3 \cdot xH_2O$), gallium nitrate hydrate (Ga $(NO_3)_3 \cdot xH_2O$), and zinc acetate dehydrate (Zn $(CH_3COO)_2 \cdot 2H_2O$) precursors were purchased from Sigma−Aldrich (St. Louis, MO, USA) and used without further purification. Human serum albumin (A1653), human lactoferrin (L1294), D-(+)-glucose (G7528), glucose oxidase from *Aspergillus niger* (G7141), β-casein from bovine milk (C6905), human lysozyme (L1667), bovine serum albumin (10775835001), fetal bovine serum (F9665), and human recombinant MMP-9 (SAE0077) were also purchased from Sigma−Aldrich (St. Louis, MO, USA). Moreover, APTES was purchased from Sigma−Aldrich and stored in a dry, ventilated place.

PBS and anhydrous ethanol were purchased from Samchun Chemical Co. (Seoul, South Korea). All other reagents and solvents were of analytical grade. Deionized (DI) water (18 MΩ cm, 25 °C) was used throughout. PDMS prepolymer (Sylgard 184A) and curing agent (Sylgard 184 B) were purchased from Dow Corning Co., Ltd. (Shanghai, China).

2.2. Aptamers. MMP-9 (5′- Phosphate-TTT TTT TTT TCG TAT GGC ACG GGG TTG GTG TTG GGT TGG-3′) and scrambled (5′-Phosphate-TGG TTG TTT GTT TGC CGT TGG AGG TCT TTG TGT TGG ATG-3′) aptamers, both 5′-phosphorylated, were purchased from Bionics (Seoul, South Korea) and purified via high-performance liquid chromatography. They were diluted in DI water to 5 μM, heated to 95 °C for 5 min, and cooled to room temperature for 30 min. Aptamer secondary structures were predicted using the RNAfold web server (http://rna.tbi.univie.ac.at).[41]

2.3. Aptamer-Binding Assays by Enzyme-Linked Aptamer-Based Sandwich Assay (ELASA). Binding assays were performed using a commercial MMP-9 ELISA kit (ElabScience, Houston, TX, USA) according to the manufacturer's instructions. The kit's biotin-conjugated antibody was replaced with an MMP-9 aptamer or scrambled aptamers to confirm binding affinity. Briefly, 100 ng/mL MMP-9 was added to antibody-coated 96-well plates and incubated for 90 min at 37 °C. Then, 5 μM MMP-9 aptamer, scrambled aptamer, or PBS solution per well was added and incubated for 1 to 4 h at room temperature. After washing four times with PBS, fluorescence intensity was measured using a Synergy HTX plate reader (BioTek, Winooski, VT, USA) and fluorescence micrographs were captured with a DP74 digital camera paired with an AX70 microscope (Olympus, Tokyo, Japan).

2.4. Preparation of IGZO Precursor. In $(NO_3)_3 \cdot xH_2O$, Ga $(NO_3)_3 \cdot xH_2O$, and Zn $(CH_3COO)_2 \cdot 2H_2O$ M at a molar ratio of 0.1:0.15:0.0275, respectively, with a total concentration of 0.1 M, were mixed in 2-methoxyethanol as an IGZO precursor. The solution was stirred at 60 °C for 4 h, then filtered through a 0.2 μm hydrophobic polytetrafluoroethylene membrane syringe filter to remove precipitates before use.

2.5. Fabrication of IGZO-EGTFT. Sensor substrates were prepared by thermal oxidation of a 300 nm-thick layer of silicon dioxide on heavily boron-doped Si wafers. Source and drain electrodes were fabricated using a combination of 5 nm titanium and 50 nm gold metal using via e-beam evaporation and photolithography. Before spin-coating the IGZO precursor solution onto the Si wafer, an oxygen plasma treatment was performed at 100 W for 10 min to transform the hydrophobic surface into a hydrophilic one. Wafers were spin-coated at 4000 rpm for 30 s, followed by annealing the coating layers at 400 °C for 1.5 h to form a dense metal-oxide-semiconductor layer. The IGZO thin film was patterned using conventional photolithography and wet-etching processes. The final sensor was passivated using epoxy-based SU-8 3008, except for the

patterned IGZO thin film. To evaluate film thickness, cross-sectional micrographs were acquired using a focused ion beam (Helios 5 UX, Thermo Fisher Scientific).

2.6. Surface Characterization. Morphologies were assessed using AFM, WCA measurements, and FT-IR. AFM images were acquired with an NX 10 (Park systems, Republic of Korea) in noncontact mode using a scanning probe with a resonance frequency of 330 kHz, a spring constant of 42 N/m, and a scan range of 5 μm. Hydrophilicity was evaluated by WCA measurements; 10 μL DI water was dropped on the center of the surface, followed by side-view photography using a digital camera (Ace acA2000-165um, Basler Cameras, Germany). Images were processed using ImageJ software. Mean contact angles were obtained from three distinct measurements. All samples were maintained at 25 °C and 30−35% humidity. The ATR mode was used for FT-IR analyses (Vertex 80v, Bruker, Germany) in the range of 1500−4000 cm^{-1}, with scanning resolution of 1 cm^{-1} and a scan number of 32.

2.7. Electrical Characterization. All sensor measurements were made using a submerged Ag/AgCl reference electrode (RE) (CHI111, Qrins, South Korea) as a gate electrode in an electrolyte solution. I−V characteristics were measured for all IGZO-EGTFTs using a Keithley 2612 B dual-channel source meter, under ambient conditions in a dark box. The normalized response (NR) of the sensor was calculated using eq 1:

$$NR = \frac{(I_D - I_0)I_0|V_G = 1 \text{ V}, \ V_D = 0.5 \text{ V}}{I_0|V_G = 1 \text{ V}, \ V_D = 0.5 \text{ V}} \quad (1)$$

where I_O and I_D are the drain currents of the IGZO-EGTFTs before and after treatments, respectively, which were ATPES treatment, aptamer immobilization, and MMP-9 recognition.

2.8. Human Participants and Samples. Tear samples were collected from 31 participants with DED. A corneal specialist (K. S. Na) examined the ocular surface using a slit-lamp microscope. Tear film instability is a key factor in DED diagnosis, with a tBUT < 5 s generally observed in patients with DED; tBUT was measured by placing sodium fluorescein paper at the lower tarsal conjunctiva. Patients were asked to blink, with time before the defect appeared in the stained tear film measured and recorded using a stopwatch. Means of three measurements were used. Exclusion criteria were: any inflammatory disease not associated with dry eyes; ocular trauma or surgical history within the previous year; pregnancy; diabetes; hypertension; rheumatologic, hematologic, and respiratory diseases; systemic infection; or any other significant systemic disease.

Tear samples were collected following topical anesthesia with 0.5% proparacaine hydrochloride eye drops (Alcaine, Alcon), with approval from the Institutional Review Board of Yeouido St. Mary's Hospital (SC24TISI0099). Informed written consent was obtained from all participants after providing detailed information about the study objectives, procedures, potential risks, and voluntary nature of participation. All procedures involving human subjects were conducted in accordance with the Declaration of Helsinki and applicable institutional and national ethical guidelines.

A bonded 2.0 × 10 mm polyester fiber rod (Transorb wicks, Filtrona, Richmond, VA, USA) provided by Professor Yong Woo Ji (Yongin Severance Hospital, Yonsei University College of Medicine, Yongin, Republic of Korea) was used to collect tears by placing it on the tear-film meniscus of the lower-lid margin of each eye for 5 min, without ocular contact or irritation. Samples were placed into sterilized 1.5 mL microcentrifuge tubes (MCT-150-C, Axygen) and clarified at 15,000 × g for 20 min at 4 °C. Samples were stored at −70 °C. MMP-9 levels were assessed using the InflammaDry test kit (Quidel Eye Health, San Diego, CA, USA). The same samples were used to quantify MMP-9 using the sensor.

2.9. Statistical Analysis. Differences were evaluated using one-way analysis of variance following equal variances using Tukey's and Duncan's tests for cross-validation. Probability (p) values indicating significance are denoted as *p < 0.05, **p < 0.01, and ***p < 0.001.
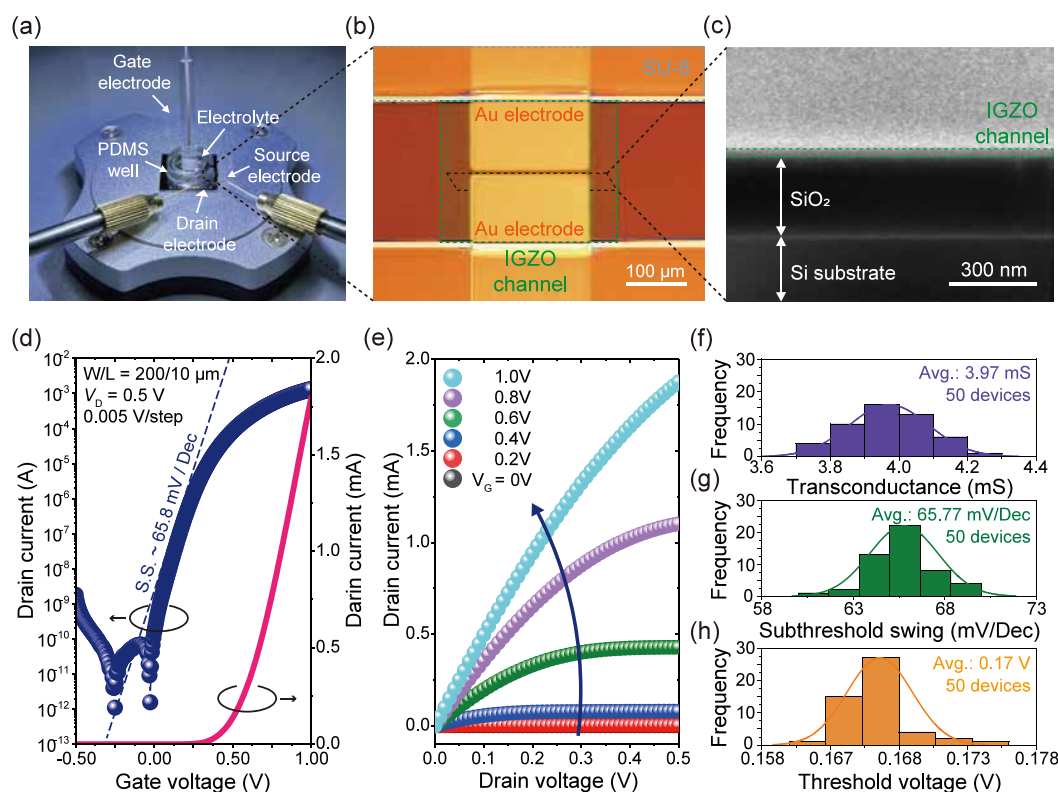
Figure 1. Electrical characteristics of IGZO-EGTFT using PBS solution. (a) Photograph showing the measurement setup of IGZO-EGTFTs fabricated on the silicon substrate (a total of 20 devices were fabricated in 15×15 mm^2). (b) Optical microscopy image of the IGZO-EGTFTs. The IGZO channel layer and an SU-8 passivation are deposited on the au electrode (source and drain) for electrical isolation. The dimensions of the IGZO channel layer are 200×10 μm. (c) Cross-sectional scanning electron microscopy (SEM) image of solution-processed IGZO channel under optimized process conditions. (d) Transfer characteristics (I_D vs V_G) measured at $V_D = 0.5$ V ($V_G = -0.5 - 1$ V), and (e) output characteristics (I_D vs V_D) of the IGZO-EGTFTs (at $V_G = 0$, 0.2, 0.4, 0.6, 0.8, and 1 V). Statistical distribution of (f) maximum transconductance (defined as gm = $\Delta I_D/\Delta V_G$), (g) subthreshold swing (S.S.), and (h) threshold voltage in PBS solution.

3. RESULTS AND DISCUSSION

3.1. MMP-9 Sensor Design and Electrical Characterizations. Figure 1a shows a photograph of the IGZO-EGTFT sensor. Sol−gel IGZO was employed as a channel material for its high current driving capability, excellent manufacturability, good size scalability, and cost effectiveness.[42−45] The source and drain (S/D) electrodes were patterned under the IGZO channel, with a large width-to-length ratio (200 μm/10 μm) to boost channel current modulation. The fabricated device is comprised of 20 thin-film transistors (TFTs) in 15×15 mm^2. Polydimethylsiloxane (PDMS) was integrated into the EGTFTs to avoid any leakage during electrical measurement; it also stabilized the potential while maintaining a consistent volume of electrolyte solution. Subsequently, a Ag/AgCl RE was positioned in the electrolyte solution as a gate electrode to prevent the formation of an EDL.

Figure 1b shows optical micrographs of the IGZO channel layer and the S/D electrodes. SU-8 was used to passivate the IGZO channel layer after it was selectively exposed within an active area of 2000 μm^2 through conventional photolithography. This passivation prevents short circuits caused by direct interaction between the electrolyte and S/D electrodes. Figure 1c shows cross-sectional scanning electron microscopy showed that thin IGZO channel layer with a thickness of 20−25 nm formed uniformly on the substrate.

A top-gate bottom-contact configuration was employed to prevent direct contact between the S/D electrodes and electrolytes as shown in Figure S1. The operational voltage

(from −0.5 to 1 V) applied to the Ag/AgCl RE caused ion migration from the electrolyte toward the IGZO channel layer, changing the electronic charge at the interface between them. This accumulation of charges forms an EDL consisting of a compact inner and outer Helmholtz layer with nanometer-scale thickness, yielding an exceptionally high capacitance (6.2 μF/cm^2).[46] A more detailed description of the fabrication process is presented in Figure S2.

Key sensor parameters were evaluated in phosphate-buffered saline (PBS) solution. Figure 1d,e show representative transfer and output curves, respectively, providing the basis for subsequent experimental design. From the transfer curve, drain currents (I_D) were monitored over gate voltages (V_G, −0.5 to 1 V) at a constant drain voltage (V_D, 0.5 V) using an Ag/AgCl RE for solution gate biasing. Impressive n-type electrical characteristics were observed at low operational voltages, including an on/off current ratio of 10^8, a transconductance of 3.97 mS (Figure 1f), a subthreshold swing of 65.77 mV/Dec (Figure 1g), and a threshold voltage (V_{TH}) of 0.17 V (Figure 1h). A small clockwise hysteresis cycle (Figure S3) was observed across >50 devices within narrow distributions.

Another crucial parameter of this sensor is its stability in biological solutions. Figure S4 shows dynamic plots of I_D as a function of V_G from 0.2 to 1 V with a constant V_D of 0.5 V, in which changes in electrical characteristics after 10^3 s of recording were negligible. This demonstrates the biological robustness of the IGZO channel layer. This duration aligned
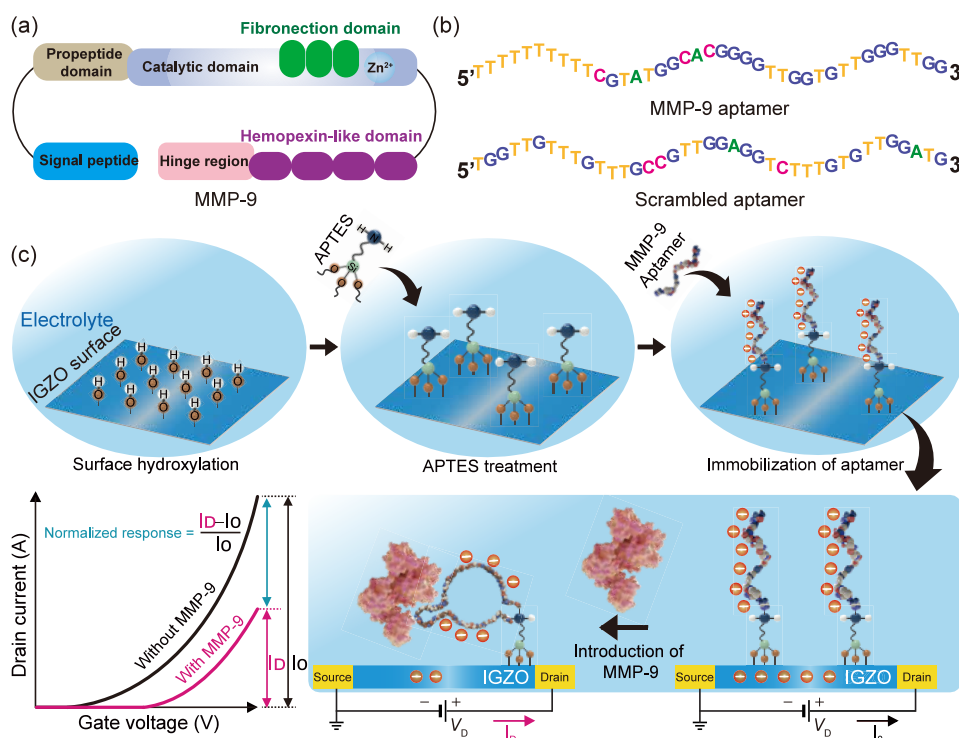
Figure 2. Design of aptamers sequence and operational mechanism. (a) Structural illustration of the domain structures and motifs of MMP-9. (b) The Illustration showing a sequence of MMP-9 and scrambled aptamer. Scrambled aptamer was used to verify the selectivity of MMP-9 sensors. (c) Surface functionalization steps to detect MMP-9 involving hydroxylation of the IGZO surface via oxygen plasma, APTES cross-linking treatment, immobilization of a specific aptamer as a bioreceptor, and direct recognition of MMP-9 in the electrolyte. In the presence of MMP-9, the aptamer-MMP-9 complex undergoes a conformational change and moves close to the IGZO sensing layer, leading to quantitative shifts in channel current. The presence of MMP-9 dramatically shifted the transfer curve in a positive direction.

with the crucial settling period required for accurate detection of biological analytes in potential applications.[47] Finally, to verify reproducibility across different fabrication conditions, IGZO-EGTFTs were fabricated in three independent batches, and devices were characterized at multiple positions on each 6-in. wafer. As shown in Figure S5, the transfer curves remained highly consistent regardless of spatial location or batch, demonstrating excellent uniformity and reproducibility of electrical performance on a large-area scale.

3.2. Operational Mechanism of MMP-9 Sensors. MMP-9 contains a signal peptide, a propeptide domain, a catalytic domain, and a flexible hinge region Figure 2a.[48] An aptamer with a major DNA sequence (5′-Phosphate-TTT TTT TTT TCG TAT GGC ACG GGG TTG GTG TTG GGT TGG-3′) was selected as the bioreceptor to specifically target MMP-9.[49] To control for nonspecific interactions, scrambled aptamers with randomized DNA sequences (5′-Phosphate-TGG TTG TTT GTT TGC CGT TGG AGG TCT TTG TGT TGG ATG-3′) of the same length were used (Figure 2b). Figure 2c illustrates 3-aminopropyltriethoxysilane (APTES) surface functionalization and aptamer immobilization. Chemical modification with APTES induced a condensation reaction between silane siloxane groups and hydroxyl groups generated on the IGZO surface by oxygen plasma treatment. To develop an aptamer-based sensing interface, modified with a 5′ phosphate, was covalently bound on the APTES-functionalized IGZO surface. To further elucidate the sensing mechanism, we noted that, in the presence of MMP-9, the aptamer underwent a specific conformational change into a compact G-quadruplex structure (Figure S6).[50] This conformational change caused the

negatively charged phosphate backbone of the aptamer to move closer to the IGZO channel surface, thereby increasing the negative charge. This mechanism is especially effective in physiological environments including PBS and tear samples, where the high ionic strength results in a short Debye length ($\sim$1 nm).[51] As a result, the potential at the interface between electrolyte and IGZO channel decreases not only leading to a shift in the effective V_{TH} and a modulation of the channel current but also providing a label-free indicator of MMP-9 concentration.

3.3. Surface Analysis of MMP-9 Sensors. To evaluate surface functionalization and recognition of MMP-9, atomic force microscopy (AFM), water contact angle (WCA), Fourier-transform infrared (FT-IR) spectroscopy, and ELASA were used. Figures 3a(i)−(iv) and S7 present the AFM images and height histograms of the IGZO surface microstructures, respectively. The pristine IGZO has a surface roughness (R_q) of $\sim$0.11 nm (Figure 3b). Following modifications with APTES and aptamer, R_q increased to 0.28 and 0.48 nm, respectively, because of the introduction of silane and aptamer molecules. This R_q increase is comparable with those reported in similar studies.[52] After drop-casting the MMP-9 solution, the R_q dramatically increased to 4.06 nm, reflecting an increment of 3.58 nm from the R_q measured in the absence of MMP-9, indicating that the aptamer and MMP-9 form complexes with obvious cluster structures.

Figure 3c and Table S1 show WCA data for the pristine IGZO surface, APTES treatment, aptamer immobilization, and direct recognition of MMP-9. The pristine IGZO surface exhibited a mean WCA of 52.45°. Following APTES treatment, this value increased to 64.99°, which can be
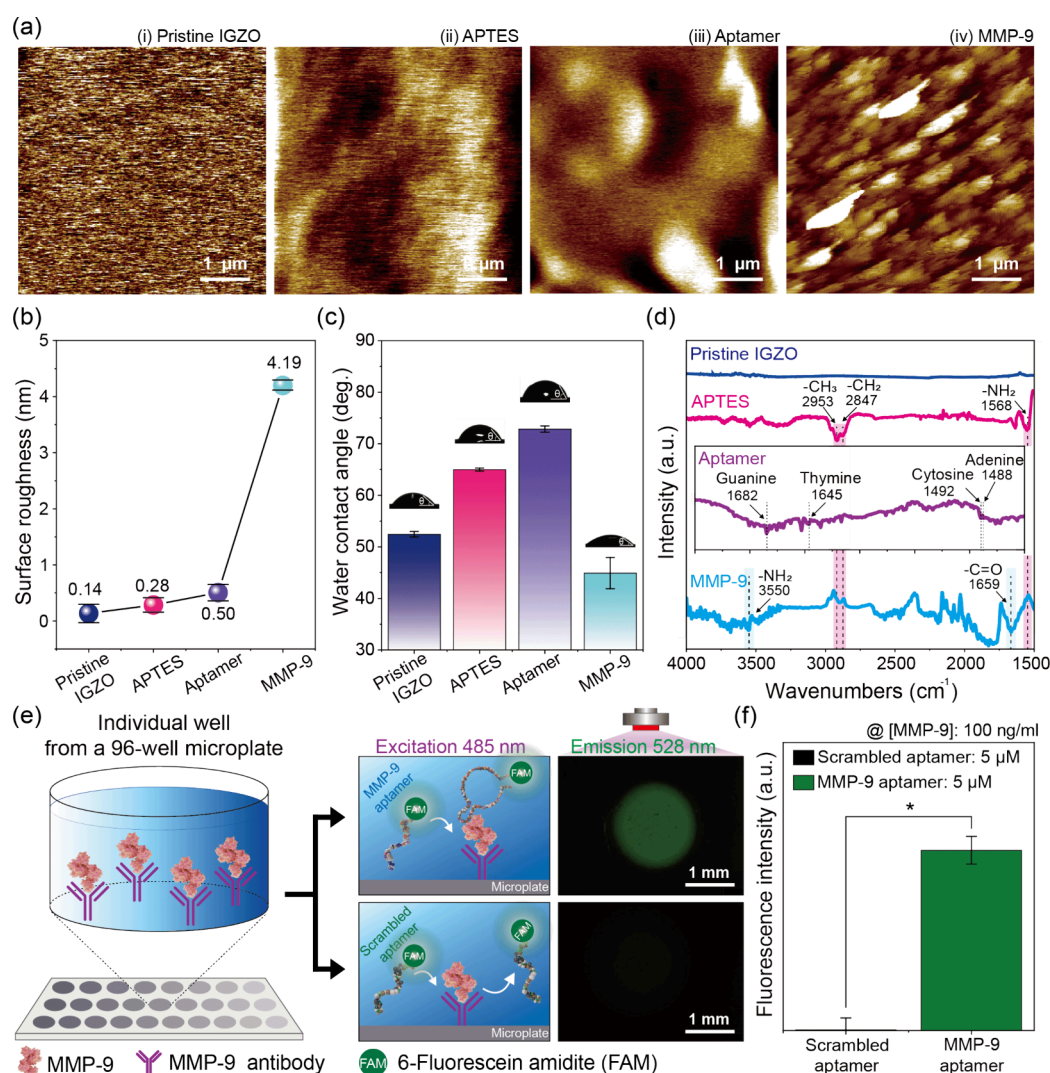
Figure 3. Surface analysis of functionalized IGZO surface. (a) The AFM surface morphologies for the surface functionalization on the IGZO surface. The AFM morphology scans (5×5 μm) acquired in noncontact mode of (i) pristine IGZO, (ii) APTES treatment, (iii) aptamer immobilization, and (iv) recognition of MMP-9. (b) Surface roughness changes according to the surface functionalization process obtained by analyzing AFM results. (c) Water droplets contact angles and (d) Fourier transform infrared (FT-IR) spectra according to surface functionalization including pristine IGZO, treatment APTES, immobilization of aptamer, and recognition of MMP-9. Based on the specific surface condition. (e) Schematic showing experimental strategy to determine aptamer-MMP-9 complex using enzyme-linked aptamer-based sandwich assay (ELASA). (f) Fluorescence intensity depends on formation of the aptamer-MMP-9 complex.

attributed to enhanced hydrophobicity after amine-terminated surface modification. The WCA further increased to approximately 72.85° after the immobilization of the aptamer. This was likely due to the hydrophobic carbon chain of the aptamer as well as consistent with prior studies using aptamers for surface functionalization.[47,48] Conversely, the WCA was significantly reduced to 44.91° upon MMP-9 introduction. This decrease can be attributed to hydrophilic functional groups, such as carboxyl and amino groups within the polypeptide chain of MMP-9, increasing surface hydrophilicity.[53,54]

FT-IR spectroscopy was performed to confirm surface functionalization (Figure 3d). After APTES treatment, a strong absorption peak corresponding to the deformation mode of the amine group was present at 1568 cm^{-1}[53], confirming the presence of silane with a free amine group. Stretching vibrations of $-CH_3$ and $-CH_2$ at 2953 and 2847 cm^{-1}[54], respectively, corresponded to the APTES backbone, consistent with its deposition on the IGZO surface. These peaks were consistently observed across all APTES concentrations ranging from 1 to 10% (Figure S8). Given that aptamers are synthetic nucleic acids, the peaks observed at 1450−1750 cm^{-1} on the aptamer-functionalized surface indicate the presence of heterocyclic compounds, providing additional evidence for covalent coupling between the aptamer and the surface. These peaks correspond well with previously reported DNA signatures for all four bases.[55−58] Following MMP-9 recognition, two peaks (1659 and 3550 cm^{-1}) were significantly reduced. The former can be attributed to the stretching vibration of the C=O bond,[59] whereas the latter is associated with the combination vibration of the NH_2 bonds.[60]

For further validation of recognizing MMP-9, an enzyme-linked aptamer-base sandwich assay (ELASA) was performed using an aptamer targeting MMP-9.[49] A scrambled aptamer with a randomized DNA sequence of the same length was used to control nonspecific interactions. Initially, both aptamers
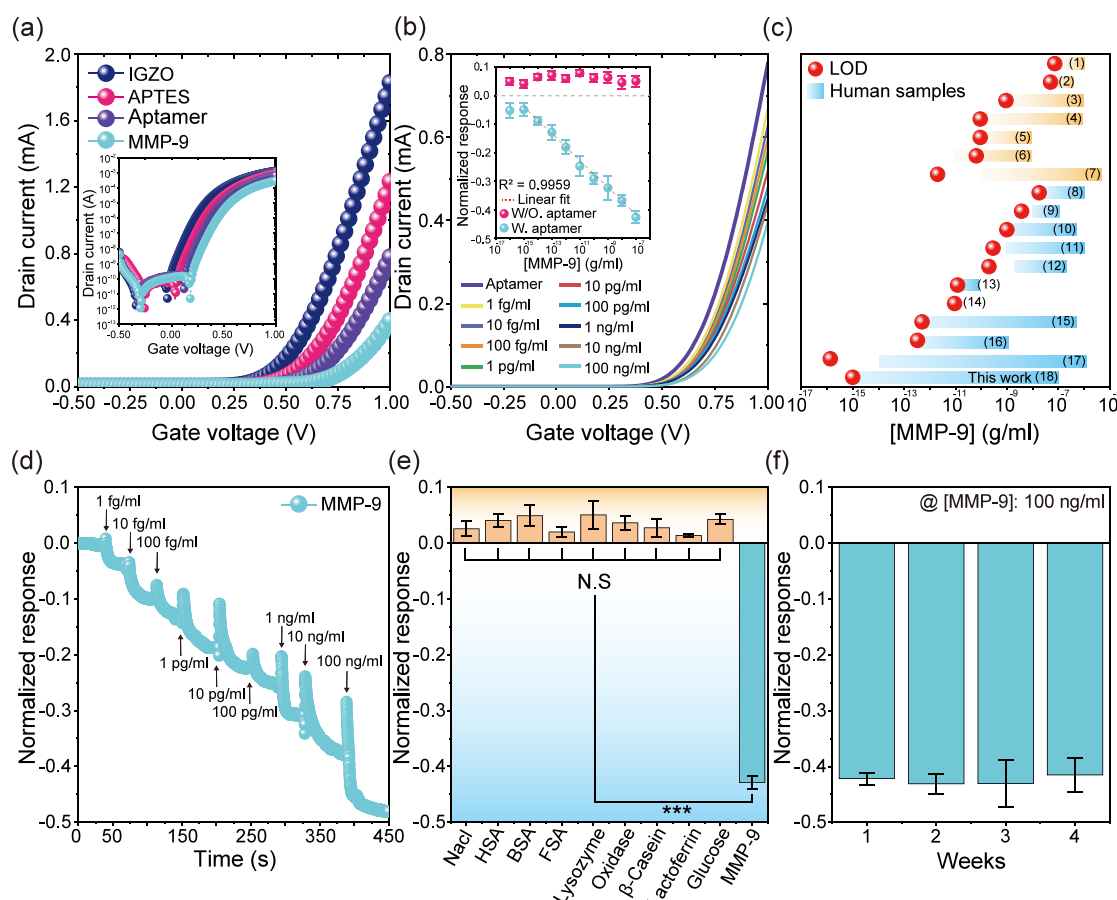
Figure 4. Electrical characteristics of the IGZO-EGTFT for detecting MMP-9. (a) Transfer characteristics of the IGZO-EGTFTs following APTES treatment, MMP-9 aptamers immobilization, and recognition of MMP-9 at a linear scale in PBS solution. The inset shows the transfer characteristics at the logarithmic scale. (b) Transfer characteristics with various concentrations of MMP-9 at the linear scale in PBS solution. The inset shows a wide detection range and the linear response for MMP-9 concentrations from 1 fg/mL to 100 ng/mL. (error bars represent standard deviation, Total $N = 144$). (c) Overview of the sensing performance including a limit of detection (LoD) and detection ranges for several types of MMP-9 detecting techniques based on the data provided in Table S2. (d) Real-time measurement of serially diluted MMP-9 concentration in a range of 1 fg/mL−100 ng/mL with aptamer-immobilized IGZO-EGTFTs. (e) Selectivity tests of the MMP-9 sensors to normal interference, including phosphate buffered saline (PBS), human, bovine serum albumin (HAS), bovine serum albumin (BSA), fatal bovine serum albumin (FSA), lysozyme, glucose oxidase from *Aspergillus niger* (oxidase), β-casein, lactoferrin, and glucose. *** indicates "significant, ($p < 0.001$)", N.S indicates "non-significant." (f) Long-term stability of sensors toward 100 ng/mL of MMP-9. After immobilizing aptamers, the sensors are stored in sealed vacuum tubes at room temperature for 4 weeks.

were labeled with the green 6-fluorescein phosphoramidite dye at their 3′ ends. Figure 3e illustrates the ELASA design. A 96-well microplate was precoated with human anti-MMP-9 antibodies. After introducing the MMP-9 and scrambled aptamers, strong fluorescence intensity was detected with only the former, indicating the formation of aptamer-MMP-9 complexes (Figure 3f). In summary, all experimental results indicate that the IGZO surface was functionalized by APTES, the aptamer in sequence, and the detection of MMP-9 successfully.

3.4. Sensor Sensitivity, Selectivity, Stability, and Reproducibility. Transfer curves (I_D-V_G) were measured after each surface functionalization step, (Figure 4a). First, the amino groups ($-NH_2$) of the APTES-deposited IGZO surface easily absorbed hydrogen ions (H^+) from the electrolyte, leading to a change in I_D. Following the covalent binding of the aptamer to APTES, the transfer curve exhibited a positive shift because the negatively charged nucleotide phosphates modulated the charge density on the functionalized surface, consistent with previous studies.[61] This trend was further

confirmed by the positive shift in V_{TH} (Figure S9). Although aptamers had a high affinity for target recognition, experimental conditions, including aptamer concentration and response time needed to be optimized to reduce the influence of unreacted active sites. Therefore, the NR value was measured over aptamer concentrations of 1−15 μM for reaction times of 1−3 h. Although aptamers have a high capacity for target recognition, experimental conditions, including concentration and response time, need to be optimized to reduce the influence of unreacted active sites. For this purpose, the NR values were measured at various aptamer concentrations ranging from 1 to 15 μM for different reaction times from 1 to 3 h. As demonstrated in Figure S10, the NR value decreases significantly with increasing aptamer concentrations and stabilizes at 5 μM. In addition, 3 h is the optimal reaction time for surface functionalization with the aptamer, as shown in Figure S11. These findings suggest that under the optimized conditions, all APTES active sites on the IGZO surface can be covalently bound with the aptamer. Considering the difficulty in collecting large volumes of tears, it
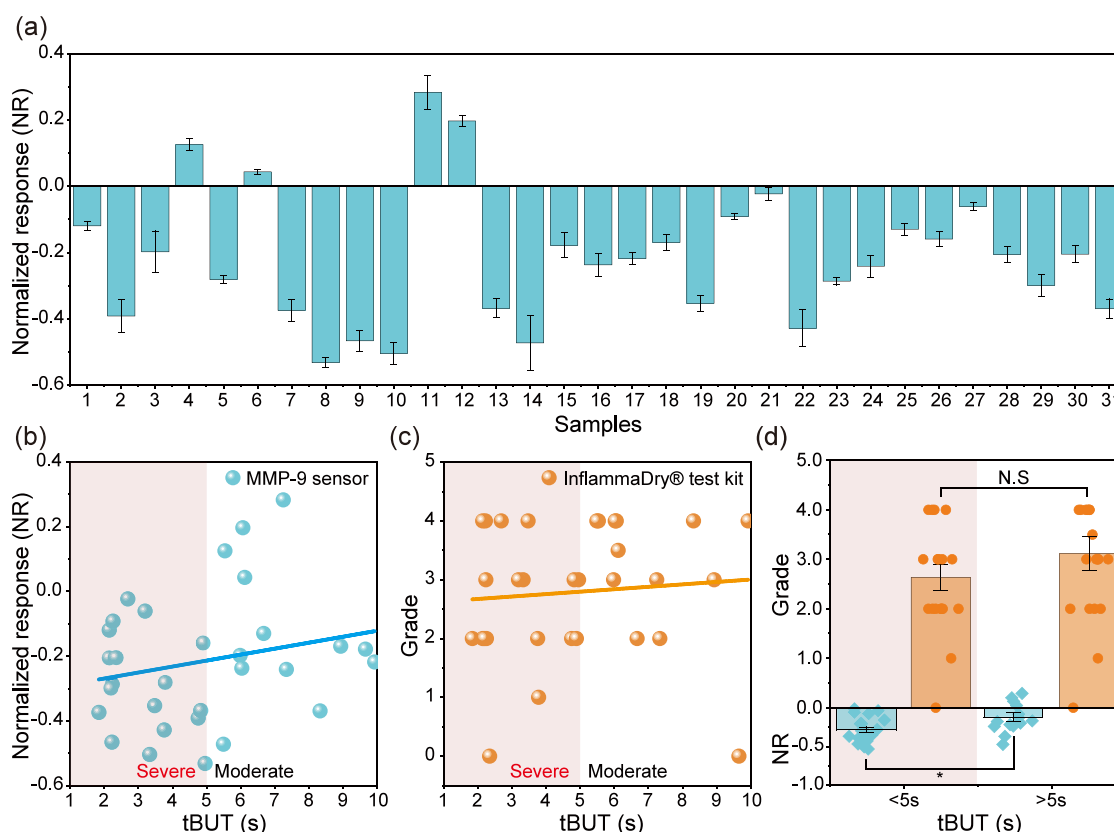
Figure 5. Validation for the MMP-9 sensors using human tear samples of dry eye patients. (a) Electrical measurement of the MMP-9 sensors to tear samples acquired from dry eye patients (error bars represent standard deviation, Total N = 31). Correlation between the detecting levels of MMP-9 and tBUT in our (b) sensors (c) or InflammaDry test kit. The slope in each graph represents the reactivity of MMP-9 proteins, which shows that the sensitivity of the sensor is superior than that of the InflammaDry test kit. (d) Comparison of the sensitivity using MMP-9 sensors and InflammaDry test kit based on clinical severity of tBUT 5 s. * indicates "significant, ($p < 0.05$)", N.S indicates "non-significant."; grade 0: negative, grade 1: trace positive, grade 2: weak positive, grade 3: positive, grade 4: strong positive.

was essential to determine the minimal sample volume; as it was reduced from 3 to 1 μL, NR value exhibited negligible changes. Further decreasing sample volume from 1 to 0.5 μL decreased NR value significantly from −0.426 to −0.335 (Figure S12). Therefore, we conclude that 1 μL is the minimum sample volume for accurate detection and minimizing false-negatives.

To determine the sensitivity of the sensor, the response of IGZO-EGTFTs to varying MMP-9 concentrations was experimentally evaluated. Transfer curves were recorded over concentrations of 1 fg/mL−100 ng/mL at a constant V_D of 0.5 V (Figure 4b). The inset shows a linear relationship between NR value and the logarithm of MMP-9 concentration with a correlation coefficient (R^2) of 0.996. The fitted equation had errors of −0.047 ± 0.00107 and −0.745 ± 0.01354 in the slope and intercept, respectively. A significant change in NR value was observed at 1 fg/mL and a theoretical limit of detection (LoD) of 1 fg/mL was also inferred from the sensitivity plot. Instead of applying the conventional $3\sigma/S$ method, we adopted a practical definition of LoD as the lowest concentration that produced a clearly distinguishable sensor response from baseline variations.

Consequently, our IGZO-EGTFT sensor exhibited an exceptionally low LoD of 1 fg/mL and a broad detection range of 1 fg/mL−100 ng/mL which outperformed the established methods reported in the literature (Figure 4c and Table S2). Figure 4d shows the change in NR values of the

IGZO-EGTFTs for the real−time monitoring of MMP-9 in PBS solution. The input voltage of the IGZO-EGTFT is biased at V_G = 1 V and V_D = 0.5 V, and the drain current is measured over time while the analyte ion concentration is varied from 1 fg/mL to 100 ng/mL. The observed decrease stepwise in NR values with increasing MMP-9 concentration aligns with the expected operational mechanism of IGZO-EGTFT for MMP-9 detection.

A key feature of an effective sensor in a clinical setting is its selectivity in the presence of structurally similar interfering biomolecules. To evaluate the selectivity of the IGZO-EGTFT sensor, the NR value and transfer curves ($I_D−V_G$) were measured in the presence of potential interfering proteins, including human serum albumin, bovine serum albumin, and fetal bovine serum. Electrical characteristics were measured in the presence of PBS, glucose oxidase from *Aspergillus niger* (oxidase), β-casein, glucose, and other biomarkers relevant to DED diagnosis, such as lactoferrin and lysozyme (Figure 4e).[62−66] Notably, our sensor exhibited a statistically significant decrease in NR ($\Delta I/I_0$ = −0.426) in response to MMP-9, whereas no significant changes in NR value were observed with any of the other biomolecules; negligible V_{TH} shifts were observed in transfer curves (Figure S13). While these results provide strong evidence of sensor selectivity, future works include comparative testing with purified MMP isoforms such as MMP-2 and MMP-7. These studies help our understanding of the structural specificity of the aptamer for target

recognition and enhance the potential utility of the aptamer in various clinical settings.

Finally, the sensor was tested after storage in sealed vacuum tubes at room temperature for 1−4 weeks after aptamer immobilization. As shown in Figure 4f, the sensor retained 96.7% of its initial performance at an MMP-9 concentration of 100 ng/mL after 4 weeks of storage. This stability can be attributed to the excellent biocompatibility of the IGZO channel and coating stability. Sensor reproducibility was investigated using seven different devices modified with aptamers over 4 weeks. As shown in Figure S14, the relative standard deviation was 3.95% for 100 ng/mL MMP-9, indicating good reproducibility. These findings underscore the applicability of the sensor in clinical applications.

3.5. Clinical Validation. The consistency, accuracy, and overall diagnostic ability of the developed sensor were compared with those obtained from the commercial InflammaDry test. Figure 5a shows NR value measured directly using human tears collected from 31 participants with DED (Table S3).

The correlation between tBUT and the measured MMP-9 concentration reveals that the NR level decreases as the tBUT is shortened. Specifically, the NR value drops below zero when the tBUT is less than 10 s, indicating that the IGZO-EGTFT sensing results reflect the degree of compromise in tear film stability (Figure 5b). In contrast, MMP-9 levels sensed by the InflammaDry test kit remained relatively consistent regardless of the decreased tBUT, typically ranging between 2 and 3 (Figure 5c). These results suggest that the IGZO-EGTFT sensor has higher sensitivity than the commercial diagnostic kit to small changes in tear-film stability, consistent with superior diagnostic capabilities.

In order to assess DED severity, NR values measured by the sensor and the ratings obtained by the test kit were analyzed (Figure 5d) for cases in which tBUT was either below or above the threshold (5 s). The sensor exhibited markedly strong responses to MMP-9 at tBUTs of <5 s. Conversely, for patients with tBUTs >5 s, the response of the sensor was considerably weak. However, the commercial diagnostic kit failed to show a significant grading difference between the two groups. These findings demonstrate that our IGZO-EGTFT sensor has excellent sensitivity for the detection of MMP-9, particularly in patients with severe dry eye symptoms. Therefore, the IGZO-EGTFT sensor can accurately detect disease progression and the severity of DED based on the sensitive detection of MMP-9 concentration.

4. CONCLUSIONS

In summary, we developed an ultrasensitive and real-time MMP-9 sensor based on sol−gel IGZO-EGTFTs. The IGZO surface was functionalized via multiple steps, and the involved binding chemistry was investigated using WCA, FT-IR, AFM and ELASA. By optimizing the experimental design, the aptamer specifically detects MMP-9, leading to stable and reliable electrical responses that were proportional to the MMP-9 concentration. This precise molecular interaction between the aptamer and the MMP-9 provides a detection limit of 1 fg/mL with a sensitivity of 47.12 μA/decade as well as a broad linear detection range from 1 fg/mL to 100 ng/mL (R^2 = 0.996). The sensor tracked variations in MMP-9 concentration dynamically, with negligible responses to interferents or nonspecific biomolecules. Finally, we confirmed long-term performance stability over 4 weeks without accuracy

degradation, highlighting its potential as a proficient MMP-9 sensor. Therefore, the present study not only demonstrates high-quality, reliable, reproducible, and quantitative data on MMP-9 detection from human tears but also provides precise diagnostic solutions for early detection and timely treatment of DED.

■ ASSOCIATED CONTENT

Ⓢ Supporting Information

The Supporting Information is available free of charge at https://pubs.acs.org/doi/10.1021/acsami.5c03926.

> Schematic diagram of the device structure; fabrication process of IGZO-EGTFTs; hysteresis measurement of the IGZO-EGTFTs; measurement of transfer characteristics at different positions in the 6-in. wafer; secondary structure of the MMP-9 aptamer; histogram of height using AFM; FT-IR spectra after treating different concentrations of APTES; change of threshold voltage shifts according to surface functionalization; change of NR against different experimental conditions of aptamer and sample volumes of MMP-9; transfer characteristics in the presence of potential interfering factors; change of NR after 4 weeks; WCA value according to surface modification; comparison of the parameters of the MMP-9 biosensor; and detailed information about patients with DED (PDF)

■ AUTHOR INFORMATION

Corresponding Authors

Kyung-Sun Na − *Department of Ophthalmology, Yeouido St. Mary's Hospital, College of Medicine, The Catholic University of Korea, Seoul 07345, Republic of Korea;* ⓘ orcid.org/0000-0003-2708-7356; Email: drna@catholic.ac.kr

Dae Yu Kim − *Department of Electrical and Computer Engineering, Inha University, Incheon 22212, Republic of Korea; Center for Sensor Systems, Inha University, Incheon 22212, Republic of Korea;* ⓘ orcid.org/0000-0003-4200-5670; Email: dyukim@inha.ac.kr

Authors

Chuljin Hwang − *Department of Electrical and Computer Engineering, Inha University, Incheon 22212, Republic of Korea;* ⓘ orcid.org/0000-0001-5646-2077

Jee Hoon Lee − *Inha Research Institute for Aerospace Medicine, Inha University, Incheon 22212, Republic of Korea;* ⓘ orcid.org/0009-0000-9581-0476

Dong-Kyu Kim − *Department of Ophthalmology, Yeouido St. Mary's Hospital, College of Medicine, The Catholic University of Korea, Seoul 07345, Republic of Korea;* ⓘ orcid.org/0000-0003-1961-7097

Complete contact information is available at:
https://pubs.acs.org/10.1021/acsami.5c03926

Author Contributions

C.H. performed formal analysis, investigation, and visualization of figures, and wrote the original draft. J.H.L. performed the biological experiments, analyzed the data, and prepared the figures. D.-K.K. performed clinical data acquisition, analysis, and interpretation. K.-S.N. performed data analysis and interpretation and primarily reviewed the manuscript. D.Y.K.

performed data analysis and interpretation, conducted project administration, and reviewed the manuscript.

Notes

The authors declare no competing financial interest.

■ REFERENCES

(1) Mehrvar, M.; Abdi, M. Recent Developments, Characteristics, and Potential Applications of Electrochemical Biosensors. *ANAL. SCI.* **2004**, *20* (8), 1113−1126.

(2) Clayton, J. A. Dry Eye. *New England Journal of Medicine* **2018**, *378* (23), 2212−2223.

(3) Craig, J. P.; Nelson, J. D.; Azar, D. T.; Belmonte, C.; Bron, A. J.; Chauhan, S. K.; de Paiva, C. S.; Gomes, J. A. P.; Hammitt, K. M.; Jones, L.; Nichols, J. J.; Nichols, K. K.; Novack, G. D.; Stapleton, F. J.; Willcox, M. D. P.; Wolffsohn, J. S.; Sullivan, D. A. TFOS DEWS II Report Executive Summary. *Ocular Surface* **2017**, *15* (4), 802−812.

(4) The Epidemiology of Dry Eye Disease: Report of the Epidemiology Subcommittee of the International Dry Eye WorkShop (2007)*Ocul. Surf.*20075293107

(5) Benítez-del-Castillo, J.; Labetoulle, M.; Baudouin, C.; Rolando, M.; Akova, Y. A.; Aragona, P.; Geerling, G.; Merayo-Lloves, J.; Messmer, E. M.; Boboridis, K. Visual Acuity and Quality of Life in Dry Eye Disease: Proceedings of the OCEAN Group Meeting. *Ocular Surface* **2017**, *15* (2), 169−178.

(6) Farrand, K. F.; Fridman, M.; Stillman, I. Ö.; Schaumberg, D. A. Prevalence of Diagnosed Dry Eye Disease in the United States Among Adults Aged 18 Years and Older. *American Journal of Ophthalmology* **2017**, *182*, 90−98.

(7) Hynnekleiv, L.; Magno, M.; Vernhardsdottir, R. R.; Moschowits, E.; Tønseth, K. A.; Dartt, D. A.; Vehof, J.; Utheim, T. P. Hyaluronic Acid in the Treatment of Dry Eye Disease. *Acta Ophthalmol.* **2022**, *100* (8), 844−860.

(8) Papas, E. B. The Global Prevalence of Dry Eye Disease: A Bayesian View. *Ophthalmic Physiologic Optic* **2021**, *41* (6), 1254−1266.

(9) Pena-Verdeal, H.; Garcia-Queiruga, J.; Sabucedo-Villamarin, B.; Garcia-Resua, C.; Giraldez, M. J.; Yebra-Pimentel, E. A Comprehensive Study on Tear Meniscus Height Inter-Eye Differences in Aqueous Deficient Dry Eye Diagnosis. *Journal of Clinical Medicine* **2024**, *13* (3), 659.

(10) Kojima, T.; Dogru, M.; Kawashima, M.; Nakamura, S.; Tsubota, K. Advances in the Diagnosis and Treatment of Dry Eye. *Progress in Retinal and Eye Research* **2020**, *78*, No. 100842.

(11) Mou, Y.; Xiang, H.; Lin, L.; Yuan, K.; Wang, X.; Wu, Y.; Min, J.; Jin, X. Reliability and Efficacy of Maximum Fluorescein Tear Break-up Time in Diagnosing Dry Eye Disease. *Sci. Rep* **2021**, *11* (1), 11517.

(12) Amparo, F.; Wang, H.; Yin, J.; Marmalidou, A.; Dana, R. Evaluating Corneal Fluorescein Staining Using a Novel Automated Method. *Investigative Ophthalmology & Visual Science* **2017**, *58* (6), BIO168−BIO173.

(13) Savini, G.; Prabhawasat, P.; Kojima, T.; Grueterich, M.; Espana, E.; Goto, E. The Challenge of Dry Eye Diagnosis. *Clin Ophthalmol* **2008**, *2* (1), 31−55.

(14) Vigo, L.; Pellegrini, M.; Bernabei, F.; Carones, F.; Scorcia, V.; Giannaccare, G. Diagnostic Performance of a Novel Noninvasive Workup in the Setting of Dry Eye Disease. *J. Ophthalmol.* **2020**, *2020*, No. 5804123.

(15) Liu, M.; Huang, L.; Liu, Y.; Yang, S.; Rao, Y.; Chen, X.; Nie, M.; Liu, X. Identification of the MMP Family as Therapeutic Targets and Prognostic Biomarkers in the Microenvironment of Head and Neck Squamous Cell Carcinoma. *Journal of Translational Medicine* **2023**, *21* (1), 208.

(16) Li, L.; Jiao, L.; Feng, D.; Yuan, Y.; Yang, X.; Li, J.; Jiang, D.; Chen, H.; Meng, Q.; Chen, R.; Fang, B.; Zou, X.; Luo, Z.; Ye, X.; Hong, Y.; Liu, C.; Li, C. Human Apical-out Nasal Organoids Reveal an Essential Role of Matrix Metalloproteinases in Airway Epithelial Differentiation. *Nat. Commun.* **2024**, *15* (1), 143.

(17) Messmer, E. M.; von Lindenfels, V.; Garbe, A.; Kampik, A. Matrix Metalloproteinase 9 Testing in Dry Eye Disease Using a Commercially Available Point-of-Care Immunoassay. *Ophthalmology* **2016**, *123* (11), 2300−2308.

(18) Zaleska-Żmijewska, A.; Strzemecka, E.; Wawrzyniak, Z. M.; Szaflik, J. P. Extracellular MMP-9-Based Assessment of Ocular Surface Inflammation in Patients with Primary Open-Angle Glaucoma. *J. Ophthalmol.* **2019**, *2019* (1), No. 1240537.

(19) Sambursky, R. Presence or Absence of Ocular Surface Inflammation Directs Clinical and Therapeutic Management of Dry Eye. *Clinical Ophthalmology* **2016**, *10*, 2337−2343.

(20) Kaufman, H. E. The Practical Detection of MMP-9 Diagnoses Ocular Surface Disease and May Help Prevent Its Complications. *Cornea* **2013**, *32* (2), 211−216.

(21) Li, C.-R. Role of Lymphotoxin Alpha as a New Molecular Biomarker in Revolutionizing Tear Diagnostic Testing for Dry Eye Disease. *Int. J. Ophthalmol.* **2023**, *16* (11), 1883−1889.

(22) Bang, S. P.; Son, M. J.; Kim, H.; Lee, Y. H.; Jun, J. H. In Vitro Validation of the Tear Matrix Metalloproteinase 9 In-Situ Immunoassay. *Sci. Rep* **2020**, *10* (1), 15126.

(23) Peng, P.; Liu, C.; Li, Z.; Xue, Z.; Mao, P.; Hu, J.; Xu, F.; Yao, C.; You, M. Emerging ELISA Derived Technologies for *in Vitro* Diagnostics. *TrAC Trends in Analytical Chemistry* **2022**, *152*, No. 116605.

(24) Hu, R.; Sou, K.; Takeoka, S. A Rapid and Highly Sensitive Biomarker Detection Platform Based on a Temperature-Responsive Liposome-Linked Immunosorbent Assay. *Sci. Rep* **2020**, *10* (1), 18086.

(25) Solier, C.; Langen, H. Antibody-Based Proteomics and Biomarker Research—Current Status and Limitations. *PROTEOMICS* **2014**, *14* (6), 774−783.

(26) Hosseini, S.; Vázquez-Villegas, P.; Rito-Palomares, M.; Martinez-Chapa, S.; Advantages, O., Disadvantages and Modifications of Conventional ELISA. In *Enzyme-linked Immunosorbent Assay (ELISA): From A to Z.*; Hosseini, S.; Vázquez-Villegas, P.; Rito-Palomares, M.; Martinez-Chapa, S. O., Eds.; Springer: Singapore, 2018; pp 67−115.

(27) Su, X.; Liu, X.; Xie, Y.; Chen, M.; Zhong, H.; Li, M. Quantitative Label-Free SERS Detection of Trace Fentanyl in Biofluids with a Freestanding Hydrophobic Plasmonic Paper Biosensor. *Anal. Chem.* **2023**, *95* (7), 3821−3829.

(28) Wan, C. J.; Liu, Y. H.; Zhu, L. Q.; Feng, P.; Shi, Y.; Wan, Q. Short-Term Synaptic Plasticity Regulation in Solution-Gated Indium−Gallium−Zinc-Oxide Electric-Double-Layer Transistors. *ACS Appl. Mater. Interfaces* **2016**, *8* (15), 9762−9768.

(29) Rim, Y. S.; Bae, S.-H.; Chen, H.; Yang, J. L.; Kim, J.; Andrews, A. M.; Weiss, P. S.; Yang, Y.; Tseng, H.-R. Printable Ultrathin Metal Oxide Semiconductor-Based Conformal Biosensors. *ACS Nano* **2015**, *9* (12), 12174−12181.

(30) Fujii, M. N.; Ishikawa, Y.; Miwa, K.; Okada, H.; Uraoka, Y.; Ono, S. High-Density Carrier-Accumulated and Electrically Stable Oxide Thin-Film Transistors from Ion-Gel Gate Dielectric. *Sci. Rep* **2016**, *5* (1), 18168.

(31) Kumar, N.; Kumar, J.; Panda, S. Enhanced pH Sensitivity over the Nernst Limit of Electrolyte Gated A-IGZO Thin Film Transistor Using Branched Polyethylenimine. *RSC Adv.* **2016**, *6* (13), 10810−10815.

(32) Ma, P.; Du, L.; Wang, Y.; Jiang, R.; Xin, Q.; Li, Y.; Song, A. Low Voltage Operation of IGZO Thin Film Transistors Enabled by

Ultrathin Al$_2$O$_3$ Gate Dielectric. *Appl. Phys. Lett.* **2018**, *112* (2), No. 023501.

(33) Wu, X.; Surendran, A.; Ko, J.; Filonik, O.; Herzig, E. M.; Müller-Buschbaum, P.; Leong, W. L. Ionic-Liquid Doping Enables High Transconductance, Fast Response Time, and High Ion Sensitivity in Organic Electrochemical Transistors. *Adv. Mater.* **2019**, *31* (2), 1805544.

(34) Du, B.; Li, Q.; Wei, J.; Liu, J. Large Area, Ultrathin, and Transparent InGaZnO Films from Printing of Liquid Ga−In−Zn Alloys for Thin Film Transistors. *ACS Appl. Nano Mater.* **2023**, *6* (19), 18083−18092.

(35) Lim, S.; Mah, D.-G.; Yoon, B.; Lee, H.; Cho, W.-J.; Park, H. Barrier Height Modulation in Amorphous IGZO/Metal Interface Using Trichlorosilane-Based Self-Assembled Monolayers. *Appl. Surf. Sci.* **2025**, *682*, No. 161693.

(36) Kim, H.; Kwon, J.-Y. Enzyme Immobilization on Metal Oxide Semiconductors Exploiting Amine Functionalized Layer. *RSC Adv.* **2017**, *7* (32), 19656−19661.

(37) Hwang, C.; Baek, S.; Song, Y.; Lee, W.-J.; Park, S. Wide-Range and Selective Detection of SARS-CoV-2 DNA via Surface Modification of Electrolyte-Gated IGZO Thin-Film Transistors. *iScience* **2024**, *27* (3), No. 109061.

(38) Syedmoradi, L.; Ahmadi, A.; Norton, M. L.; Omidfar, K. A Review on Nanomaterial-Based Field Effect Transistor Technology for Biomarker Detection. *Microchim Acta* **2019**, *186* (11), 739.

(39) Chae, M.-S.; Park, J. H.; Son, H. W.; Hwang, K. S.; Kim, T. G. IGZO-Based Electrolyte-Gated Field-Effect Transistor for in Situ Biological Sensing Platform. *Sens. Actuators, B* **2018**, *262*, 876−883.

(40) Zhang, H.; Wu, M.; Ta, H. T.; Xu, Z. P.; Zhang, R. Recent Development and Applications of Sensors for the Detection of Matrix Metalloproteinases. *Advanced Materials Technologies* **2023**, *8* (9), 2201786.

(41) Gruber, A. R.; Lorenz, R.; Bernhart, S. H.; Neuböck, R.; Hofacker, I. L. The Vienna RNA Websuite. *Nucleic Acids Res.* **2008**, *36* (suppl_2), W70−W74.

(42) Liu, Y.; Yu, Y.; Li, T.; Hu, Y.; Unnithan, R.; Skafidas, E. High Performance and High Yield Solution Processed IGZO Thin Film Transistors Fabricated with Low-Temperature Annealed Hafnium Dioxide Gate Dielectric. *Adv. Elect Materials* **2023**, *9* (11), 2300415.

(43) Kim, J.; Park, J.; Yoon, G.; Khushabu, A.; Kim, J.-S.; Pae, S.; Cho, E.-C.; Yi, J. Effect of IGZO Thin Films Fabricated by Pulsed-DC and RF Sputtering on TFT Characteristics. *Materials Science in Semiconductor Processing* **2020**, *120*, No. 105264.

(44) Nathan, A.; Kumar, A.; Sakariya, K.; Servati, P.; Sambandan, S.; Striakhilev, D. Amorphous Silicon Thin Film Transistor Circuit Integration for Organic LED Displays on Glass and Plastic. *IEEE Journal of Solid-State Circuits* **2004**, *39* (9), 1477−1486.

(45) Shin, Y.; Kim, S. T.; Kim, K.; Kim, M. Y.; Oh, S.; Jeong, J. K. The Mobility Enhancement of Indium Gallium Zinc Oxide Transistors via Low-Temperature Crystallization Using a Tantalum Catalytic Layer. *Sci. Rep* **2017**, *7* (1), 10885.

(46) Hwang, C.; Kwak, T.; Kim, C.-H.; Kim, J. H.; Park, S. Quantitative and Rapid Detection of Iodide Ion via Electrolyte-Gated IGZO Thin-Film Transistors. *Sens. Actuators, B* **2022**, *353*, No. 131144.

(47) Arlett, J. L.; Myers, E. B.; Roukes, M. L. Comparative Advantages of Mechanical Biosensors. *Nat. Nanotechnol.* **2011**, *6* (4), 203−215.

(48) Vandooren, J.; Van den Steen, P. E.; Opdenakker, G. Biochemistry and Molecular Biology of Gelatinase B or Matrix Metalloproteinase-9 (MMP-9): The next Decade. *Crit. Rev. Biochem. Mol. Biol.* **2013**, *48* (3), 222−272.

(49) Scarano, S.; Dausse, E.; Crispo, F.; Toulmé, J.-J.; Minunni, M. Design of a Dual Aptamer-Based Recognition Strategy for Human Matrix Metalloproteinase 9 Protein by Piezoelectric Biosensors. *Anal. Chim. Acta* **2015**, *897*, 1−9.

(50) Arroyo-Currás, N.; Dauphin-Ducharme, P.; Scida, K.; Chávez, J. L. From the Beaker to the Body: Translational Challenges for Electrochemical. *Aptamer-Based Sensors. Anal. Methods* **2020**, *12* (10), 1288−1310.

(51) Nakatsuka, N.; Yang, K.-A.; Abendroth, J. M.; Cheung, K. M.; Xu, X.; Yang, H.; Zhao, C.; Zhu, B.; Rim, Y. S.; Yang, Y.; Weiss, P. S.; Stojanović, M. N.; Andrews, A. M. Aptamer−Field-Effect Transistors Overcome Debye Length Limitations for Small-Molecule Sensing. *Science* **2018**, *362* (6412), 319−324.

(52) Barua, A.; White, R. J.; Leedy, K. D.; Jha, R. Ultra-Low-Power Neurotransmitter Sensor Using Novel "Click" Chemistry Aptamer-Functionalized Deep Subthreshold Schottky Barrier IGZO TFT. *MRS Commun.* **2021**, *11* (3), 233−243.

(53) Bini, R. A.; Marques, R. F. C.; Santos, F. J.; Chaker, J. A.; Jafelicci, M. Synthesis and Functionalization of Magnetite Nanoparticles with Different Amino-Functional Alkoxysilanes. *J. Magn. Magn. Mater.* **2012**, *324* (4), 534−539.

(54) Aspinall, S. R.; Khutoryanskiy, V. V. Surface Modification of Silica Particles with Adhesive Functional Groups or Their Coating with Chitosan to Improve the Retention of Toothpastes in the Mouth. *Langmuir* **2023**, *39* (4), 1677−1685.

(55) Tsuboi, M.; Takahashi, S.; Harada, I. CHAPTER 11 - Infrared and Raman Spectra of Nucleic Acids—Vibrations in the Base-Residues. In *Structural Studies on Nucleic Acids and Other Biopolymers*; Duchesne, J., Ed.; Academic Press, 1973; pp 91−145.

(56) Dagneaux, C.; Liquier, J.; Taillandier, E. FTIR Study of a Nonclassical dT10*dA10-dT10 Intramolecular Triple Helix. *Biochemistry* **1995**, *34* (45), 14815−14818.

(57) Tsuboi, M. Application of Infrared Spectroscopy to Structure Studies of Nucleic Acids. *Appl. Spectrosc. Rev.* **1970**, *3* (1), 45−90.

(58) Zhizhina, G. P.; Oleinik, E. F. Infrared Spectroscopy of Nucleic Acids. *Russ. Chem. Rev.* **1972**, *41* (3), 258.

(59) Monajati, M.; Tavakoli, S.; Abolmaali, S. S.; Yousefi, G.; Tamaddon, A. Effect of PEGylation on Assembly Morphology and Cellular Uptake of Poly Ethyleneimine-Cholesterol Conjugates for Delivery of Sorafenib Tosylate in Hepatocellular Carcinoma. *Bioimpacts* **2018**, *8* (4), 241−252.

(60) Deng, B.; Ma, B.; Ma, Y.; Cao, P.; Leng, X.; Huang, P.; Zhao, Y.; Ji, T.; Lu, X.; Liu, L. Doxorubicin and CpG Loaded Liposomal Spherical Nucleic Acid for Enhanced Cancer Treatment. *J. Nanobiotechnol* **2022**, *20* (1), 140.

(61) Chen, C.-P.; Ganguly, A.; Lu, C.-Y.; Chen, T.-Y.; Kuo, C.-C.; Chen, R.-S.; Tu, W.-H.; Fischer, W. B.; Chen, K.-H.; Chen, L.-C. Ultrasensitive in Situ Label-Free DNA Detection Using a GaN Nanowire-Based Extended-Gate Field-Effect-Transistor Sensor. *Anal. Chem.* **2011**, *83* (6), 1938−1943.

(62) Sen, D. K.; Sarin, G. S. Tear Glucose Levels in Normal People and in Diabetic Patients. *Br J. Ophthalmol* **1980**, *64* (9), 693−695.

(63) Ohashi, Y.; Ishida, R.; Kojima, T.; Goto, E.; Matsumoto, Y.; Watanabe, K.; Ishida, N.; Nakata, K.; Takeuchi, T.; Tsubota, K. Abnormal Protein Profiles in Tears with Dry Eye Syndrome. *American Journal of Ophthalmology* **2003**, *136* (2), 291−299.

(64) Velos, P.; Cherry, P. M. H.; Miller, D. An Improved Method for Measuring Human Tear Lysozyme Concentration. *Archives of Ophthalmology* **1985**, *103* (1), 31−33.

(65) Zhang, Y.; Yan, P.; Tang, H.; Zhang, J. Rapid Detection of Tear Lactoferrin for Diagnosis of Dry Eyes by Using Fluorescence Polarization-Based Aptasensor. *Sci. Rep* **2023**, *13* (1), 15179.

(66) Duan, H.; Peng, S.; He, S.; Tang, S.-Y.; Goda, K.; Wang, C. H.; Li, M. Wearable Electrochemical Biosensors for Advanced Healthcare Monitoring. *Adv. Sci.* **2025**, *12*, No. 2411433.